Optics Letters

Dual-mode subwavelength trapping by plasmonic tweezers based on V-type nanoantennas

Ren-Chao Jin,[1] Jia-Qi Li,[1] Lin Li,[2] Zheng-Gao Dong,[1,*] and Yongmin Liu[2,3,4]

[1]Physics Department, Southeast University, Nanjing 211189, China
[2]Department of Mechanical and Industrial Engineering, Northeastern University, Boston, Massachusetts 02115, USA
[3]Department of Electrical and Computer Engineering, Northeastern University, Boston, Massachusetts 02115, USA
[4]e-mail: y.liu@northeastern.edu
*Corresponding author: zgdong@seu.edu.cn

Received 12 November 2018; revised 6 December 2018; accepted 6 December 2018; posted 10 December 2018 (Doc. ID 351211); published 9 January 2019

We propose novel plasmonic tweezers based on silver V-type nanoantennas placed on a conducting ground layer, which can effectively mitigate the plasmonic heating effect and thus enable subwavelength plasmonic trapping in the near-infrared region. Using the centroid algorithm to analyze the motion of trapped spheres, we can experimentally extract the value of optical trapping potential. The result confirms that the plasmonic tweezers have a dual-mode subwavelength trapping capability when the incident laser beam is linearly polarized along two orthogonal directions. We have also performed full-wave simulations, which agree with the experimental data very well in terms of spectral response and trapping potential. It is expected that the dual-mode subwavelength trapping can be used in non-contact manipulations of a single nanoscale object, such as a biomolecule or quantum dot, and find important applications in biology, life science, and applied physics.

https://doi.org/10.1364/OL.44.000319

Non-contact methods of trapping micro-/nano-objects are of great importance for manipulation of tiny particles that are either delicate and easily damaged, or too small to be selectively handled in a mechanical way. Optical tweezers show unique features in noninvasive manipulation of various objects [1], including micro-/nano-scaled colloidal particles, bacterial and metallic particles, and DNA [2–7]. Generally, optical tweezers use a focused laser beam to generate optical gradient fields nearby the focal spot, at which the rapid divergence of the optical fields leads to a radial gradient force to trap an object [2]. However, traditional optical tweezers suffer from several issues [8,9]. For example, the trapping force decreases rapidly with the size of trapped particles (following r^3 law, where r is the radius of the particle). Therefore, in order to overcome the Brownian motion, high laser fluence is necessary to trap small particles, which may damage the trapped particles due to the laser heating effect [8]. Additionally, the trapping position of optical tweezers cannot be precisely controlled down to the subwavelength scales due to the optical diffraction limit. These facts impose significant barriers for the applications of optical tweezers.

The rapid progress in the field of nano optics has stimulated the development of near-field optical tweezers to circumvent the issues existing in conventional optical tweezers [10–28]. In particular, researchers have investigated plasmonic tweezers based on different metallic nanostructures, such as plasmonic disks [10–15], nano-holes [16], nanoantennas [17], and even nanostructured arrays for multi-particle trapping or transport [20]. It is known that metallic nanostructures support localized surface plasmon (LSP) resonances, which can efficiently squeeze light down to the subwavelength regime and thus enhance the local field intensity. Such unique properties enable plasmonic tweezers to break the diffraction limits in conventional optical tweezers. Consequently, nanosized objects, such as single protein [16] and 10-nm-diameter metallic particles [17], have been successfully manipulated by plasmonic tweezers. Moreover, optical trapping with high spatial resolution has been realized using sophisticated nanostructures. Examples include 230-nm super-resolution optical trapping and three-dimensional optical manipulation of single 50-nm dielectric objects by engineering a bowtie plasmonic aperture at the extremity of a tapered metal-coated optical fiber [20,21]. Optical trapping by plasmonic tweezers can be more efficient if they are suitably designed to achieve selective trapping, for instance, via changing the polarization of the incident laser [18]. Plasmonic tweezers even hold the promise for on-chip optical manipulation devices, such as a nano-conveyor belt [22–24], to transport nanoparticles over a long distance.

However, several disadvantages of plasmonic tweezers need to be addressed for more practical applications. First, metallic nanostructures at the scale of 100 nm or below are usually required for plasmonic tweezers [17], which imposes significant demands on nano-fabrication. Second, the undesired optothermal effect could be enhanced by LSP resonances, which may influence the trapping efficiency and damage the sample to be trapped. Therefore, it is highly desired to realize easy-to-fabricate, heat-resistant, and even dual-mode selective plasmonic tweezers, as demonstrated in this work.

We propose and demonstrate new plasmonic tweezers based on silver V-type nanoantennas patterned on a silver ground

layer, which is schematically shown in Fig. 1(a). The silver ground layer has three-fold functions. First, it induces a significant blue shift of the LSP resonance wavelength, leading to a magnified scale of the V-type antennas, in comparison with the case in which the conventional conducting material indium-tin-oxide (ITO) is used as the ground layer. Therefore, our design greatly mitigates the nanofabrication challenge. Second, the silver ground layer can optimize the near-field distribution for trapping by lifting the strong local field to the top surface of the V-type nanoantenna, providing an optimized near-field distribution for trapping [14]. Third, it can act as a homogeneous conducting layer similar to ITO for fabrication of V-type nanoantennas, while the optothermal effect can be significantly suppressed due to the high thermal conductivity of silver [14,15].

As shown in Fig. 1(a), the antenna design consists of double head-to-head V-type nanostructures. The geometric parameters as marked are arm length $a = 450$ nm, width $b = 170$ nm, thickness $t = 120$ nm, angle between two arms $\theta = 60°$, tip gap $g = 40$ nm (i.e., head-to-head distance), and periodicity $p = 1200$ nm. For sample fabrication, we first sputtered a 20-nm-thick silver ground layer on a cleaned coverslip, and then used electron beam lithography to fabricate the V-type nanoantenna. Figure 1(b) shows the scanning electron microscope (SEM) image of the fabricated V-type nanoantennas. It is noted that the gaps between heads and tails of adjacent V-type nanoantennas determine how the local plasmonic field is enhanced and where the nanoparticle can be trapped precisely in subwavelength positions. For our nanoantenna design, there are two kinds of gaps, i.e., head-to-head and tail-to-tail gaps, as indicated in the insets in Fig. 1(b). They correspond to two LSP resonant modes that are responsible for two different trapping configurations, when the incident light is linearly polarized along horizontal and vertical directions, respectively.

Reflectance spectra were measured by placing the sample in a microfluidic chamber, and then illuminating it by linearly polarized light. Experimental results are shown in Fig. 2. In Fig. 2(a), the polarization of incident light is along the horizontal direction (parallel to the x axis), and the resulting spectral dip at 1064 nm (black line) indicates an LSP resonance of the nanoantenna array (defined as mode I). This result agrees well with simulation data (squared red line), performed by the finite-difference time-domain (FDTD) software, Lumerical Solutions. Meanwhile, Fig. 2(b) shows the measured and simulated data when the polarization is switched to the vertical direction (parallel to the y axis). Another LSP resonance (defined as mode II) emerges around 1000-nm wavelength in simulation

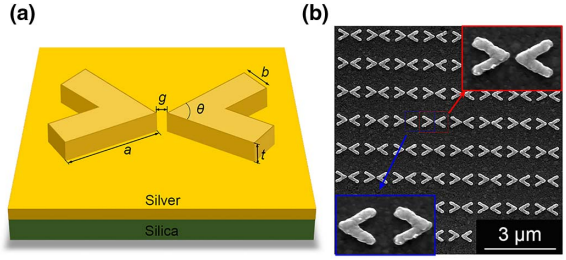

Fig. 1. (a) Perspective view of the plasmonic tweezers based on V-type nanoantenna. (b) SEM images of the fabricated nanoantennas. The insets at the top right and bottom left show the two kinds of gaps, i.e., head-to-head and tail-to-tail gaps, respectively.

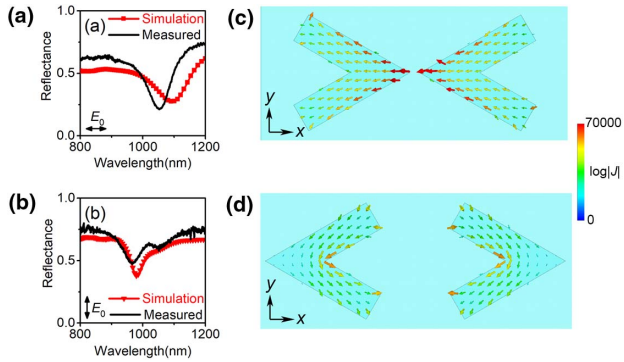

Fig. 2. Measured and simulated reflectance of the nanoantenna arrays when the incident light is polarized along (a) x axis and (b) y axis, respectively. (c), (d) Current density for plasmonic resonant modes I and II, respectively.

(triangular red line), corresponding to a reflectance dip in the measured reflectance spectrum (black line). In addition, Figs. 2(c) and 2(d) present the distribution of induced current density for modes I and II, respectively.

Subsequently, we conducted the optical trapping experiments by a homebuilt setup, which is schematically illustrated in Fig. 3. In order to avoid any unexpected influences from the environment, a closed chamber was designed to enclose the nanoantenna sample in liquid (deionized water). The chamber is shown by the inset in Fig. 3. 1-μm-diameter polystyrene spheres dispersed in solution were used as objects to be trapped. A continuous-wave laser operating at the wavelength of 1064 nm was used as the trapping laser and incident normally to the frontside of the nanoantenna array through an object lens with high magnification (100×, 0.8 NA). The power density impinging on the nanoantenna was estimated to be around 0.3 mW/μm^2. A polarizer was used to control the polarization state of the incident beam, and a beam expander was adopted to magnify the beam diameter. White light was illuminated from the backside of the sample for imaging purpose, and both reflected trapping beam and transmitted white light were collected by the object lens and finally captured by a CCD camera.

To quantitatively investigate the trapping effect of our plasmonic tweezers, the centroid algorithm was used to extract the centroid motion of a single sphere trapped by the V-type nanoantenna [20]. The motion was recorded by the CCD camera

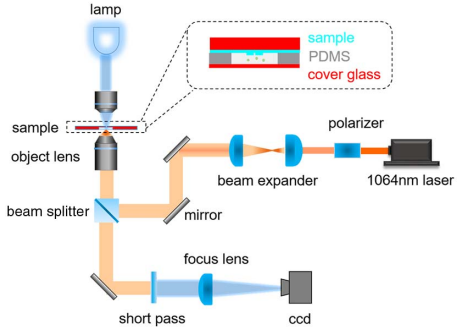

Fig. 3. Schematic of the optical setup for the optical trapping experiment. The inset at the top right shows details of the microfluidic chamber.

with a frame rate of 30 Hz. The centroid distribution of the trapped sphere represents the random Brownian motion, which has been used as an effective experimental method to probe arbitrary force fields [20]. We have calculated the trapping potential $U(r)$ acting on the particle using Boltzmann probability density function $p(r) = \exp(-U(r)/k_BT)/Z$, where Z is the partition function that normalizes the probability density function, k_B is the Boltzmann constant, and T denotes the absolute temperature [11]. The retrieved trapping potential enables us to check the unique trapping phenomena of our plasmonic tweezers compared with conventional optical tweezers.

Figure 4(a) presents the experimentally extracted trapping potential of mode I from the CCD-recorded particle motion (see Visualization 1), in which the incident laser was polarized along the x axis. Interestingly, the 2D potential well with a minimum value of $-3.97k_BT$ occupies approximately a spot of 400 nm × 150 nm area in the x–y plane, implying subwavelength manipulation. To better understand this result, we employed Lumerical FDTD solution to calculate both the near-field properties of our antenna array and the trapping potential experienced by a 1-μm-sized polystyrene sphere above the V-type nanoantenna. Figure 4(b) shows the distribution of the electric field at the plane 10 nm above the nanoantenna. The electric field enhancement around the head-to-head gap reaches up to 30 folds, manifesting a pronounced trapping potential caused by the large field gradient nearby the nanogap. Moreover, the optical trapping potential was simulated by adding a dielectric sphere (diameter $d = 1$ μm, and refractive index $n = 1.59$) above the nanoantenna. We estimated the interval between the bottom of the trapped sphere and the top surface of the nanoantenna as about 30 nm, considering the typical Debye length for electrostatic interations [18,19]. By setting the incident power intensity in the simulation to be 0.3 mW/μm^2 as estimated earlier in the experiment, we calculated the optical force exerted on the dielectric sphere at arbitrary positions in the x–y plane based on the Maxwell's stress tensor (MST) method [27]. Finally, the trapping potential was calculated by integral formula $U(r) = \int f(r)\mathrm{d}r$, where $f(r)$ denotes the optical force. Figure 4(c) shows the calculated trapping potential within a 600 nm × 600 nm area in the x–y plane, where the trapping potential minima appeared at position (0, 0) for both experimental and numerical results in Figs. 4(a) and 4(c), respectively, consistent with the maximum enhancement of electric field in the nanogap [Fig. 4(b)]. Due to the random Brownian motion of trapped spheres in experiments, the distance between sphere and nanoantenna kept changing, while in the calculation, the distance between sphere and nanoantenna was fixed. This leads to the discrepancy of the amplitude of trapping potential between experimental and calculated results.

It is interesting to investigate the trapping characteristic of mode II if the polarization of the incident laser is rotated by 90°, in which case the local field will be confined in the vicinity of the tail-to-tail gaps. The trapping potential map at this LSP resonant wavelength is again extracted from the centroid distribution of a single sphere (see Visualization 2), and the result is plotted in Fig. 5(a). Apparently, the experimental trapping potential map for mode II (minima about $-3.31k_BT$) is quite different in comparison with that for mode I. In particular, the potential well is broadened. In fact, for mode II, the local field around the head tip has a negligible enhancement, while there are strongly localized fields around the two tail-to-tail nanogaps [Fig. 5(b)], corresponding to the 440-nm separation between potential minima along the y direction. Therefore, it can be found from the centroid distribution of the trapped sphere that the motion area of the trapped sphere is obviously enlarged as compared with the case of mode I, indicating a less confined trapping area. This is easy to understand, since there are totally four tail-based hotspots separated by about 300 nm. Nevertheless, the extracted potential-well area (about 600 nm × 600 nm) from the experimental data is still much smaller in both length and width scales than the incident wavelength of 1064 nm. As a result, we can conclude that a subwavelength trapping effect is achieved for both modes I and II. Following the same procedure as described before, we have calculated the optical force for resonant mode II by MST method and obtained the trapping potential. In Fig. 5(c), the numerically calculated trapping potential map shows the minimum value of about $-5.5k_BT$ in the tail-to-tail trapping regime, and the two trapping potential minima along the y axis in Fig. 5(c) match experimental results in Fig. 5(a) very well. Note that due to the background Brownian motion of spheres and/or the optothermal effect, for both incident configurations, the experimentally extracted minimum trapping potentials (about $-3k_BT$) are higher than the calculated ones (about $-6k_BT$).

It is interesting to study the performance of our plasmonic tweezers on trapping of smaller particles. However, the experiment is challenging based on our optical setup, because of the resolution limitation of the CCD camera. Usually, the trapping of nanoparticles can be observed by monitoring the change in voltage of an avalanche photodiode [21]. Therefore, in the following, we will focus on the numerical calculation of the optical trapping potential maps of an Au nanosphere and a polystyrene sphere (both with diameters of 20 nm) by our plasmonic

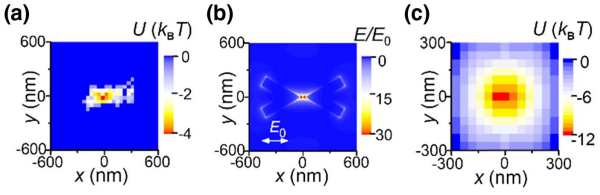

Fig. 4. (a) Experimentally retrieved trapping potential from the centroid motion of a single particle trapped under x-polarized laser beam, with incident intensity of 0.3 mW/μm^2. (b) Simulated distribution of electric field in the x–y plane 10 nm above the top surface of nanoantenna, when the normally incident 1064-nm laser beam is polarized along the x axis. (c) Calculated trapping potential map for a 1-μm-diameter dielectric sphere.

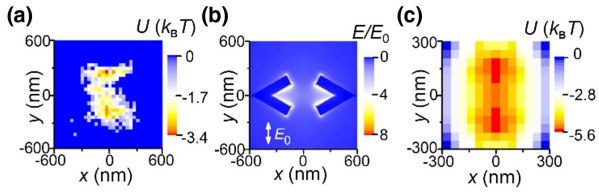

Fig. 5. (a) Experimentally retrieved trapping potential under y-polarized laser beam, with incident intensity of 0.3 mW/μm^2. (b) Simulated distribution of electric field in the x–y plane 10 nm above the top surface of nanoantenna, when the normally incident 1064-nm laser beam is polarized along the y axis. (c) Calculated trapping potential map for a 1-μm-diameter dielectric sphere.

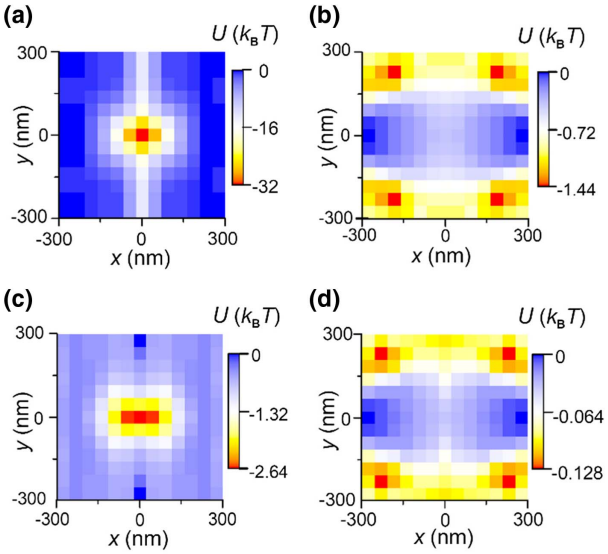

Fig. 6. Simulated optical trapping potential for a 20-nm-diameter Au sphere with (a) x- and (b) y-polarized illuminations. Simulated optical trapping potential for a 20-nm-diameter polystyrene sphere with (c) x- and (d) y-polarized illuminations. The power density is 40 mW/μm^2 in the simulation.

tweezers, respectively. The gap between the nanoantenna and nanosphere is set to be 10 nm. Figures 6(a) and 6(b) represent the trapping capability for an Au nanosphere using mode I and mode II, respectively. The trapping potential map for mode I [Fig. 6(a)] indicates that the Au nanosphere could be trapped and immobilized at position (0,0) with a potential of $-32k_BT$, which is 10 times larger than the reported potential result of trapped Au nanospheres (estimated to be $-3.84k_BT$ with the same diameter) subjected to similar illumination power density [28]. Figure 6(b) demonstrates that the trapping potential map for a 20-nm-diameter Au nanosphere agrees well with the near-field distribution of the nanoantenna for mode II. Moreover, the trapping potential maps for a 20-nm-diameter polystyrene sphere for mode I and mode II are shown in Figs. 6(c) and 6(d), respectively. Similarly, the potential maps show the dual-mode subwavelength trapping capability. However, the values of trapping potential minimum for a 20-nm-diameter Au nanosphere is about 10 times larger than those for a polystyrene sphere because of the higher polarizability of gold.

Due to the diffraction limit, conventional optical tweezers based on far-field trapping encounter obstacles at the nanoscale, hampering their applications for occasions that require subwavelength accuracy. We have designed novel plasmonic tweezers using metallic V-type nanoantennas patterned on a uniform metal ground layer, which can significantly benefit optical trapping in several aspects, including significantly enlarging the structural scales with an infrared trapping beam, suppressing the plasmonic heat issue, as well as dual-mode, subwavelength trapping by simply switching the polarization. This dual-mode subwavelength trapping capability, demonstrated by Boltzmann statistics of centroid motion of the trapped particle, is attributed to different local-field enhancements under excitations of horizontal and vertical linear polarizations of the incident beam, respectively. The experimental trapping results have been further confirmed by FDTD numerical simulations with good consistence. This subwavelength plasmonic trapping shows great potentials in biomedical, microfluid, and opto-mechanical applications.

Funding. National Natural Science Foundation of China (NSFC) (11774053); Natural Science Foundation of Jiangsu Province (BK 20181263, BK 20160878).

REFERENCES

1. A. Ashkin, J. M. Dziedzic, J. E. Bjorkholm, and S. Chu, Opt. Lett. **11**, 288 (1986).
2. D. G. Grier, Nature **424**, 810 (2003).
3. T. L. Min, P. J. Mears, L. M. Chubiz, C. V. Rao, I. Golding, and Y. R. Chemla, Nat. Methods **6**, 831 (2009).
4. A. Lehmuskero, P. Johansson, H. Rubinsztein-Dunlop, L. Tong, and M. Käll, ACS Nano **9**, 3453 (2015).
5. M. Daly, M. Sergides, and S. Nic Chormaic, Laser Photon. Rev. **9**, 309 (2015).
6. Y. Yuan, Y. Lin, B. Gu, N. Panwar, S. C. Tjin, J. Song, J. Qu, and K. T. Yong, Coord. Chem. Rev. **339**, 138 (2017).
7. J. W. Black, M. Kamenetska, and Z. Ganim, Nano Lett. **17**, 6598 (2017).
8. M. L. Juan, N. Righini, and R. Quidant, Nat. Photonics **5**, 349 (2011).
9. O. M. Maragò, P. H. Jones, P. G. Guccidardi, G. Volpe, and A. C. Ferrari, Nat. Nanotechnol. **8**, 807 (2013).
10. M. Righini, A. S. Zelenina, C. Girard, and R. Quidant, Nat. Phys. **3**, 477 (2007).
11. M. Righini, G. Volpe, C. Girard, D. Petrov, and R. Quidant, Phys. Rev. Lett. **100**, 186804 (2008).
12. L. Huang, S. J. Maerkl, and O. J. F. Martin, Opt. Express **17**, 6018 (2009).
13. A. N. Grigorenko, N. W. Roberts, M. R. Dickinson, and Y. Zhang, Nat. Photonics **2**, 365 (2008).
14. K. Wang, E. Schonbrun, P. Steinvurzel, and K. B. Crozier, Nat. Commun. **2**, 469 (2011).
15. J. C. Ndukaife, A. V. Kildishev, A. G. A. Nnanna, V. M. Shalaev, S. T. Wereley, and A. Boltasseva, Nat. Nanotechnol. **11**, 53 (2016).
16. Y. Pang and R. Gordon, Nano Lett. **12**, 402 (2012).
17. W. Zhang, L. Huang, C. Santschi, and O. J. F. Martin, Nano Lett. **10**, 1006 (2010).
18. J. H. Kang, K. Kim, H. S. Ee, Y. H. Lee, T. Y. Yoon, M. K. Seo, and H. G. Park, Nat. Commun. **2**, 582 (2011).
19. C. Min, Z. Shen, J. Shen, Y. Zhang, H. Fang, G. Yuan, L. Du, S. Zhu, T. Lei, and X. Yuan, Nat. Commun. **4**, 2891 (2013).
20. Y. Tanaka, S. Kaneda, and K. Sasaki, Nano Lett. **13**, 2146 (2013).
21. J. Berthelot, S. S. Acimovic, M. L. Juan, M. P. Kreuzer, J. Renger, and R. Quidant, Nat. Nanotechnol. **9**, 295 (2014).
22. G. Wang, Z. Ying, H. Ho, Y. Huang, N. Zou, and X. Zhang, Opt. Lett. **41**, 528 (2016).
23. P. Hansen, Y. Zheng, J. Ryan, and L. Hesselink, Nano Lett. **14**, 2965 (2014).
24. Y. Zheng, J. Ryan, P. Hansen, Y. Cheng, T. Lu, and L. Hesselink, Nano Lett. **14**, 2971 (2014).
25. Y. Zhao, A. A. E. Saleh, M. A. Haar, B. Baum, J. A. Briggs, A. Lay, O. A. Reyes-Becerra, and J. A. Dionne, Nat. Nanotechnol. **12**, 1055 (2017).
26. T. Kudo, H. Ishihara, and H. Masuhara, Opt. Express **25**, 4655 (2017).
27. X. Yang, Y. Liu, R. F. Oulton, X. Yin, and X. Zhang, Nano Lett. **11**, 321 (2011).
28. M. Jiang, G. Wang, W. Jiao, Z. Ying, N. Zou, H. Ho, T. Sun, and X. Zhang, Opt. Lett. **42**, 259 (2017).